journal

Model of Strength Degradation from Hertzian Contact Damage in Tough Ceramics

Brian R. Lawn,* Seung Kun Lee,*,† Irene M. Peterson,*,‡ and Sataporn Wuttiphan

Materials Science and Engineering Laboratory, National Institute of Standards and Technology,
Gaithersburg, Maryland   20899

A model of strength degradation for ceramics subject to damage from contact with hard spheres is developed. Primary attention is focused on tough ceramics with heterogeneous microstructures which deform in a quasi-plastic mode. Brief consideration is also given to ideally brittle ceramics which form classical ring cracks, as a comparative baseline. Strength vs indentation load data from two microstructurally controlled ceramics, silicon nitride and a micaceous glass-ceramic, illustrate distinctive strength degradation responses: in fine-grain (*F*) form, ideally brittle failure from ring cracks, with abrupt strength loss at the critical load for crack initiation followed by a slow falloff at increasing load; in coarse-grain (*C*) form, failure from within the quasi-plastic zone, with continuous strength loss beyond a load well above that for the onset of yield, and with even slower falloff. Failure in the latter materials occurs from contact-induced microdamage flaws with two essential elements: an inner closed shear crack with frictional sliding faces ("shear fault"), which forms within the confining compression–shear contact field; an outer annular, kinked crack that initiates at the fault edges ("wing crack"), and that extends in tensile local mode. The critical fault–crack is modeled as a virtual crack, with the residual field from the inner fault stabilizing the net driving force on the outer wing crack during ensuing tensile loading. Finite element modeling is used to evaluate the nonlinear elastic–plastic contact fields, and to provide a relationship between residual shear fault stress and contact load. The model accounts for the essential qualitative and quantitative features of the strength–load data, with provision for catastrophic degradation at high fault densities and extreme loads by microcrack coalescence. The model also contains the ingredients for analysis of contact fatigue, via attrition of the frictional tractions on the residual fault.

I. Introduction

CONTACTS between curved surfaces, exemplified in Hertzian tests with spherical indenters, constitute an important form of loading in many ceramic-based structures, including ceramic bearings,[1,2] ceramic engine components,[3] and biochemical structures (ceramic dental restoratives,[4] hip prostheses). Above some critical load, depending on the radius of curvature of the

contacting surfaces, the ceramic structures sustain irreversible damage that can compromise their useful lifetime. The nature of this contact damage changes fundamentally as the ceramic becomes coarser and more heterogeneous, and consequently tougher, undergoing a "brittle–to–quasi-plastic" transition:[5–10] in fine-grain, homogeneous microstructures classical ring or cone cracks form in the region of weak tension outside the contact; in coarse-grain, heterogeneous microstructures diffuse microdamage forms in the region of strong compression–shear beneath the contact. In the latter case the strong stress gradients in the compression field ensure localization of the microdamage within a well-defined near-field quasi-plastic zone. At the microstructural level, the damage consists of shear-activated microcracks,[5,7,8,10,11] with two basic elements: "closed" sliding facets, "shear faults" or mode II cracks with internal frictional resistance, which form at weak grain or interphase boundaries;[12] "extensile" microcracks, mode I "wing cracks," which initiate at some kink angle from the fault edges.[13–17] At extreme high loads or number of repeat contacts neighboring microcracks may coalesce, resulting ultimately in material disintegration within the damage zone,[9] with strong implications in wear and machining.[18]

An issue of importance in the context of design is the effect that such brittle–to–quasi-plastic transitions have on the strength of ceramics after contact damage has been sustained. In ideally brittle homogeneous materials abrupt strength losses occur beyond the critical load for cone crack initiation, with continued but slower losses at increasingly higher loads. The strength degradation in this class of structure has been well analyzed in terms of conventional fracture mechanics.[19–23] No such analysis exists for tough heterogeneous ceramics—in these materials strength losses are not apparent until the load is well beyond the "yield" point for the onset of quasi-plasticity, and are thereafter continuous and even more gradual.[7,10,24] Generally, the natural strength of heterogeneous ceramics is lower than that of homogeneous ceramics, despite any increased toughness, but may remain higher after indentation—the degradation is considerably less, i.e., the material is more damage tolerant. This relatively benign response in heterogeneous structures is consistent with the notion that failure occurs from a single shear fault within the damage zone, at least up to the point of coalescence, where strength losses begin to accelerate.[9]

In this paper we construct a simple model for strength degradation from Hertzian contacts in tough, heterogeneous ceramics. For the sake of completeness, we first summarize existing models for failure from ring cracks in homogeneous structures,[19–23] with a minor modification to provide an improved prediction. For the heterogeneous structures, failure is taken to occur from an individual wing crack at the edge of a critical individual fault within the contact microdamage zone. A model is thereby developed for the degraded strength as a function of contact load. The model takes into account the contribution of residual shear stresses at the fault interface (determined by the frictional tractions) to the driving force on the ensuing extensile wing crack. In both damage modes we treat the critical microcracks as center-loaded penny cracks,

with the actual cracks growing as annular rings about virtual centers. Experimental data from two well-characterized ceramic systems, silicon nitride[24] and a micaceous glass-ceramic,[25] are used as a basis for testing the validity of the model. These material systems may usefully be prepared with effectively homogeneous and heterogeneous microstructures. Stress analysis of the contact stress field using a finite element algorithm[26] is an important adjunct to the modeling in the heterogeneous structures. The model contains provision for crack coalescence between neighboring faults at very high contact loads (or number of cycles), with accelerated degradation; and for progressive fatigue or wear, by attrition of internal friction at the sliding shear fault interface.

II. Experimental Background

In this section we summarize essential Hertzian contact test results from other studies on two ceramic materials which show definitive transitions in contact response from brittle to quasi-plastic with coarsening microstructure. The materials are silicon nitride (Si_3N_4)[24] and a machinable micaceous glass-ceramic (MGC) supplied by Corning (Corning Co., NY),[25,27–30] the first relatively hard and the second relatively soft. These two materials are readily transformed from "fine" (F) to "coarse" (C) states by simple heat treatments, yielding the coarsened and elongated rod (Si_3N_4) and platelet (MGC) microstructures indicated in Table I.

Hertzian contact tests conducted on the Si_3N_4 and MGC materials in air, using tungsten carbide spheres, produce the damage patterns shown in Figs. 1 and 2. The micrographs are half-surface and section views from "bonded-interface" ceramographic specimens.[4,24] In the F microstructures (Figs. 1(a) and 2(a)), characteristic cone cracks are formed outside the contact. A slight depression within the surface ring crack trace is observed in F-MGC (Fig. 2(a)), indicating limited quasi-plasticity even in the fine-grain state of this relatively soft material.[30] In the C microstructures (Figs. 1(b) and 2(b)), well-developed quasi-plastic damage zones are formed beneath the contact. Cone cracking is suppressed, although vestigial ring crack traces are observed on the harder C-Si_3N_4 surfaces (Fig. 1(b)). Scanning electron microscopy indicates that the damage zones consist of shear-activated microfailures at or near the interfaces between the rods in the Si_3N_4[10] or platelets in the MGC[7,30] and the second phase, i.e., "shear faults," with attendant microcracks extending into the matrix at the higher contact loads.

These two distinct modes of contact damage lead to fundamentally different strength properties. Surface micrographs of failures from Hertzian indentation sites in Si_3N_4 and MGC bars broken in four-point flexure are shown in Figs. 3 and 4. In the F microstructures (Figs. 3(a) and 4(a)) the break initiates from the base of the ring cracks, indicating a brittle failure. In the C microstructures (Figs. 3(b) and 4(b)) the break originates closer to the contact center, traversing the contact peripheries almost orthogonally, indicating failure from the subsurface quasi-plasticity zone.

Strengths σ_F are plotted as a function of contact load P for Si_3N_4[31] (WC sphere radius $r = 2.38$ mm) and MGC[25] ($r = 3.18$ mm) in Figs. 5 and 6. The data points are experimental test results: solid symbols represent failures from contact sites; open symbols represent failures from extraneous flaws. Shaded boxes at the left axes represent natural strengths from breaks on unindented specimens, means and standard deviations for a minimum of 10 tests. Vertical dashed lines indicate critical loads at the onset of fully penetrant cone cracking, P_C, and of yield, P_Y, measured independently by detecting the first indications of indentation damage on polished surfaces.[24,25] Also indicated, for the coarse structures (Figs. 5(b) and 6(b)), is the load at which strength degradation first occurs, P_D. Note that in F-Si_3N_4 (Fig. 5(a)) $P_C \ll P_Y$ ($P_Y > 5000$ N, off scale), confirming a highly brittle material, whereas in F-MGC (Fig. 6(a)) $P_Y < P_C$, consistent with a softer material. In both F materials, however, the strength loss is abrupt at $P = P_C$, consistent with failure from dominant ring cracks (Figs. 3(a) and 4(a))—the preceding yield in F-MCG is not sufficient to deter brittle fracture. Thereafter, the strength falls off slowly with increasing load, as the ring cracks increase in size.[24,25] In both C structures, $P_Y \ll P_C$ (P_C off scale), but strength loss does not occur until P_D is well above P_Y, even though failure originates from dominant quasi-plastic zones (Figs. 3(b) and 4(b)). Again, the subsequent degradation is gradual, notwithstanding an ever-expanding damage zone at increasing loads.[24,25]

The solid curves in Figs. 5 and 6 are theoretical fits to the data, to be described later in Section V.

III. Fine Microstructures: Failure from Cone Cracks

In this section we briefly review the mechanics of failure from ring cracks in brittle, fine-grain ceramics. We draw on earlier treatments,[19,23] adding a minor modification to allow for the fact that the cracks in Figs. 1(a) and 2(a) are not full, but truncated, cones.

Above a critical contact load $P = P_C$ a ring crack pops in abruptly from a surface flaw.[32,33] The crack geometry is shown schematically in Fig. 7. The dimension c of the actual ring crack is related to the dimension C of a "virtual" cone with its tip located above the contact surface:

$$C = c + R_0/\cos \alpha_0 \qquad (1)$$

where R_0 is the surface ring radius and α_0 the angle between cone crack and specimen surface. Our aim is to derive an expression for the strength of a material containing such a crack.

The stress-intensity factor for this virtual cone crack system can be well approximated by a simple relation for pennylike cracks.[24,34] For materials governed by a single-valued toughness $K_{IC} = T_0$, as befits fine-grain structures, this relation is

$$K = \chi P/C^{3/2} = T_0 \qquad (2)$$

with χ a crack geometry coefficient.[33,35] The parameter χ can

Table I. Microstructures of Ceramics Used in This Study

Material	Grain structure	Concn (vol%)	Morphology	Grain size (μm)
F-Si_3N_4	α-Si_3N_4	75	Equiaxed	0.4
	β-Si_3N_4	15	Elongate–rods	1.5×0.4
	Oxynitride glass	10	Bonding phase	
C-Si_3N_4	β-Si_3N_4	90	Elongate–rods	9×1.5
	Oxynitride glass	10	Bonding phase	
F-MGC	Mica	55	Platelets	0.3×1.0
	Fluorosilicate glass	45	Bonding phase	
C-MGC	Mica	55	Platelets	1.2×8
	Fluorosilicate glass	45	Bonding phase	

(a)

(b)

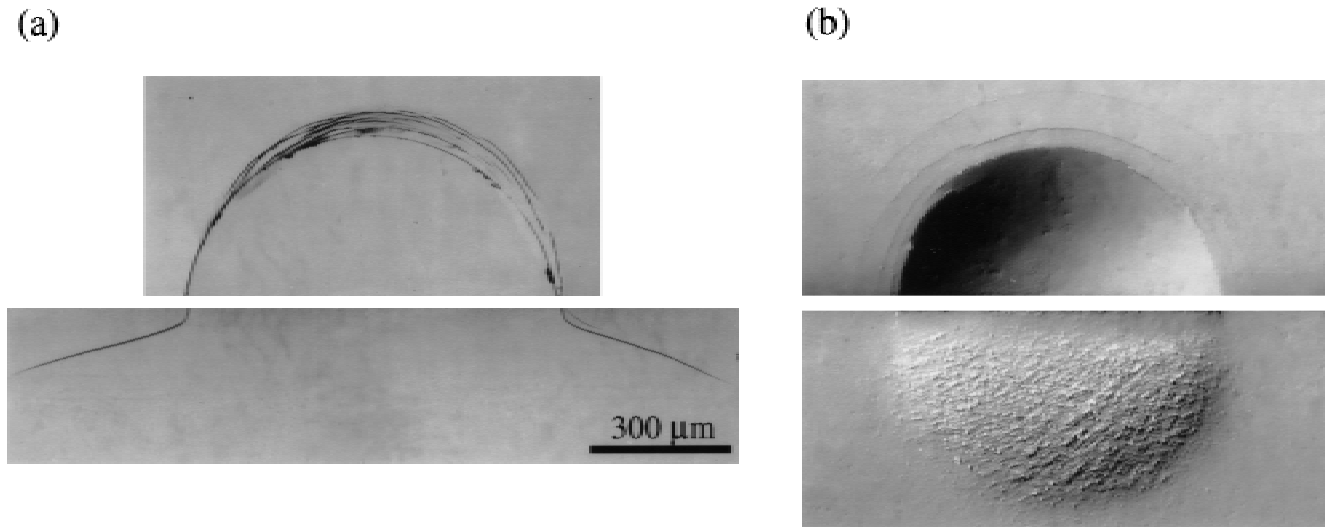**Fig. 1.** Half-surface and side views of Hertzian contact damage in silicon nitrides: (a) fine-grain F-Si$_3$N$_4$, (b) coarse-grain C-Si$_3$N$_4$. Indentations with WC sphere radius $r = 1.98$ mm at load $P = 4000$ N. Note transition from fracture-dominated to plasticity-dominated damage. Nomarski optical micrographs, bonded-interface specimens. (From Ref. 24.)

be calibrated from measurements of equilibrium cone crack lengths at specified loads, $C = (\chi P/T_0)^{2/3}$.

In the absence of any significant residual stresses associated with the indentation damage zone, failure occurs unstably from a dominant flaw according to the Griffith strength relation

$$\sigma_F = T_0/\Psi c^{1/2} \tag{3}$$

with Ψ a geometry coefficient. At $P < P_C$, σ_F is governed by the size of preexisting natural flaws, $c = c_f$, and is equal to the natural (pre-indentation) strength, σ_0, independent of P. At $P > P_C$, the strength is governed by the size c of the developed ring crack, determinable from Eqs. (1) and (2). In this region, σ_F is dependent on P, but the dependence is slow ($P^{-1/3}$ in the asymptotic limit $C \gg R_0/\cos \alpha_0$), and is only slowly dependent on r, through R_0. The coefficient $\Psi(\alpha)$ for a ring crack of

specified angle α_0 is predeterminable from a detailed fracture mechanics analysis of crack reinitiation from the cone base in tensile fields[19] (Appendix A).

The earlier analyses[19,23] neglect the truncation of the cone by treating C and c in Eq. (1) as identical, a condition that is not well satisfied unless $c \gg R_0$.

IV. Coarse Microstructures: Failure from Shear Faults

Now consider the case of tough, coarse-grain ceramics of primary interest here, where failure occurs from the microdamage zone beneath the spherical indenter. Suppose that this microdamage zone consists of a distribution of shear faults, well spaced so that overlap with neighbors does not occur at any
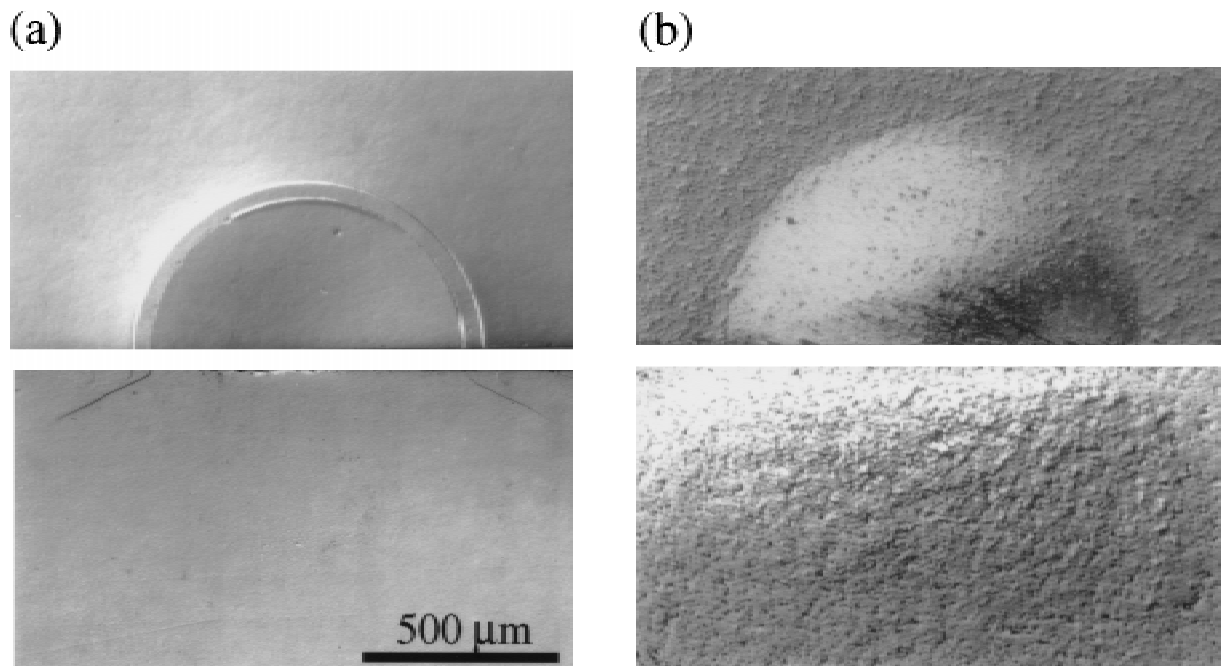
(a)

(b)

Fig. 2. Half-surface and side views of Hertzian contact damage in machinable glass-ceramics: (a) fine-grain F-MGC, (b) coarse-grain C-MGC. Indentations with WC sphere radius $r = 3.18$ mm at load $P = 1000$ N. Note transition from fracture-dominated to plasticity-dominated damage pattern. Nomarski optical micrographs, bonded-interface specimens. (From Ref. 25.)
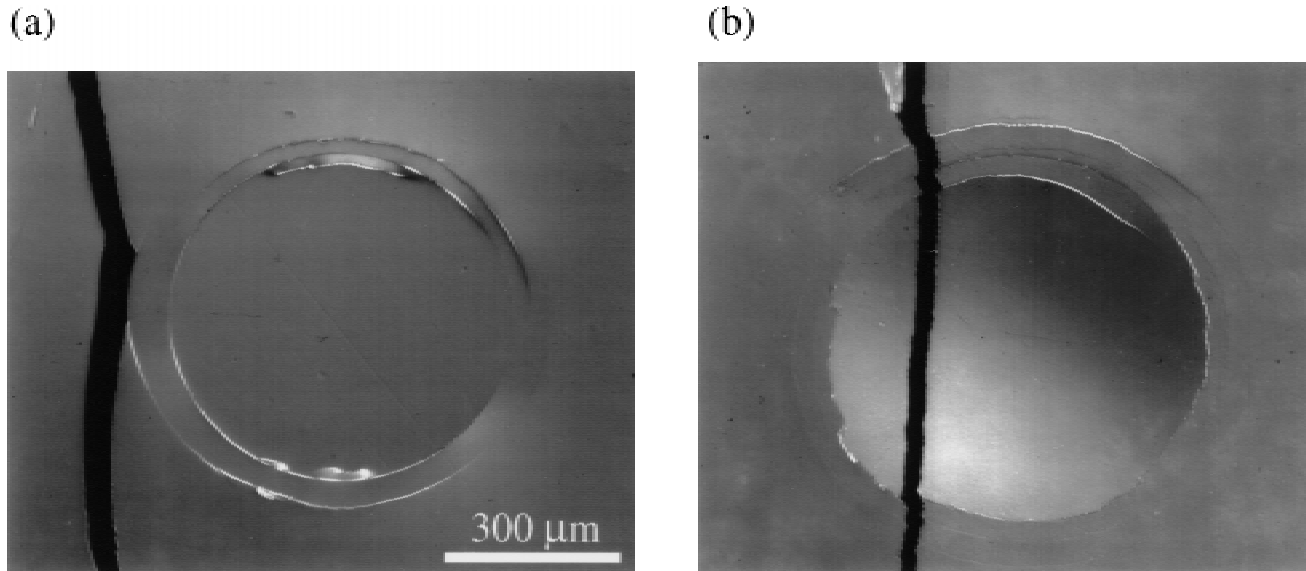
Fig. 3. Surface views of contact failure sites in silicon nitride specimens: (a) F-Si$_3$N$_4$, (b) C-Si$_3$N$_4$. Indentations with WC sphere $r = 2.38$ mm at load $P = 4000$ N. Nomarski optical micrographs, four-point bend-strength specimens, tension axis horizontal.

stage during the loading history. (We will consider the case where the fault density is high enough to cause overlap later in Section VI). Failure can then be assumed to occur from a single critical fault within the damage zone, as depicted in Fig. 8. The critical fault is taken to be located below the surface along the contact axis, oriented at 45° to this axis, where the shear stress is maximum.[26] When this maximum shear stress exceeds some threshold level, the fault surfaces slide over each other, concentrating the stresses at the fault edges. The ensuing extensile wing crack is considered to extend at 45° to the fault plane, normal to the specimen surface, so that it experiences maximum tension in the subsequent flexure field. This configuration idealizes the optimum geometry somewhat, especially in regard to the angle of the wing crack,[14,15] but captures the essence of the problem with minimum geometrical complication.

In the following analysis we shall assume that the crack lengths at failure are sufficiently small that toughness can again be taken as single-valued, corresponding to some representa-

tive value T_0 in the short-crack region of any toughness curve. As we shall see (Section V(2)), the strength relation for coarse microstructures can be reduced to normalized form in load P, eliminating any explicit dependence on T_0. Because of the relative complexity of the wing-crack geometry, we shall encounter several configurational parameters en route to this strength relation. The normalization procedure will eliminate the need to predetermine these parameters, reducing the data fitting to adjustment of just one unknown load quantity.

(1) Residual Shear Stress at Sliding Fault

Consider the response of a shear fault within a small volume element in the damage field, such that the stresses within the element are uniform and compressive. Solutions for uniform stress states can be used to provide constitutive stress–strain relations for analysis of the much more complex nonuniform, nonlinear and triaxial contact fields,[12] using numerical (FEM) procedures.[26]

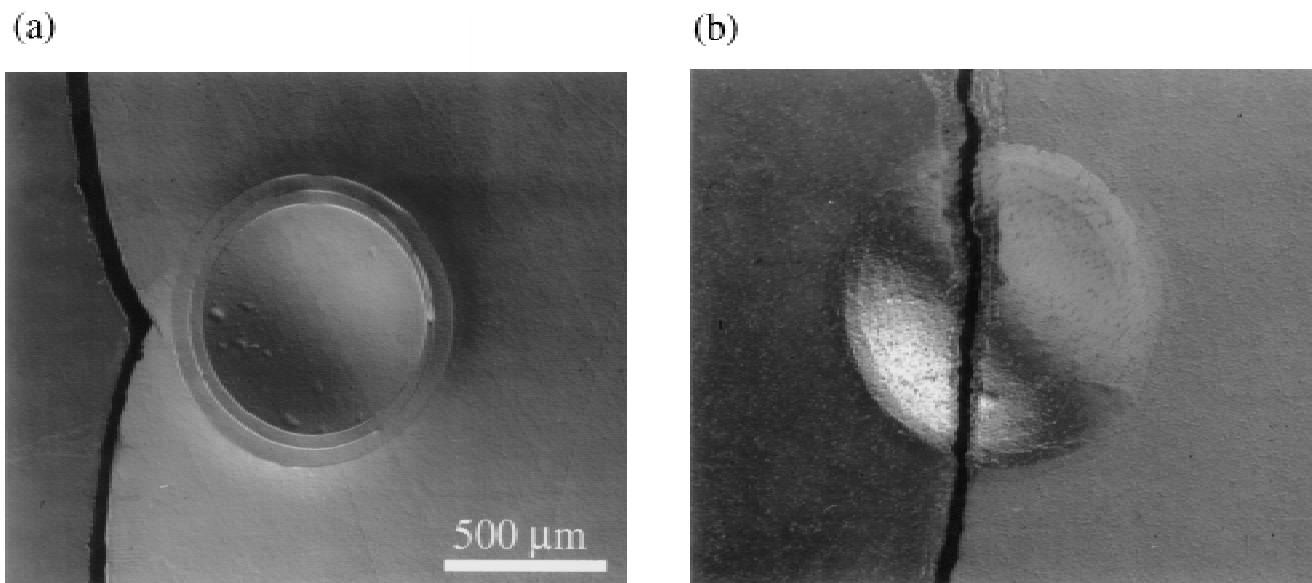**Fig. 4.** Surface views of contact failure sites in glass-ceramic specimens: (a) F-MGC, (b) C-MGC. Indentations with WC sphere $r = 3.18$ mm at load $P = 1000$ N. Nomarski optical micrographs, four-point bend-strength specimens, tension axis horizontal.
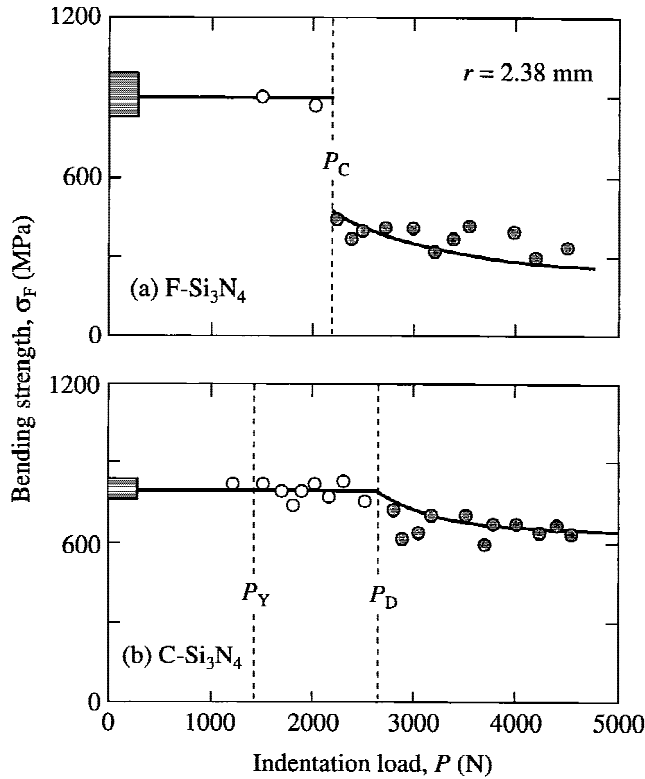
Fig. 5. Strength degradation of Hertzian-indented silicon nitrides as function of contact load: (a) *F*-Si$_3$N$_4$, failure from ring cracks; (b) *C*-Si$_3$N$_4$, failure from shear faults. Indentations with WC sphere, *r* = 2.38 mm. Four-point bend-strength specimens, 3 mm × 4 mm × 25 mm, with polished surfaces and chamfered and polished edges. Tests in fast loading (<10 ms) in inert environment (silicone oil) to avoid slow crack growth effects. Data points are individual experimental measurements: closed symbols represent failures from indentation origins, open symbols from other origins. Shaded box at left axis represents strengths of polished, unindented specimens. Vertical dashed lines indicate threshold loads P_C for cracking, P_Y for yield, and P_D for first degradation. Solid curves are theoretical fits.

The critical fault in the contact field at peak load *P* in Fig. 8 is subject to a net shear stress

$$\tau_* = \tau_P - \tau_f$$
$$= \tau_P - (\tau_c + \mu\sigma_*) \qquad (4)$$

where τ_P is the resolved shear stress on the fault plane and τ_f is a friction resistance stress, with τ_c a "cohesion" stress, μ a friction coefficient, and σ_* the resolved compression stress normal to the fault plane.[14,36] (The sign of τ_f in Eq. (4) reverses on unloading.) The condition $\tau_* > 0$, $\tau_P > \tau_f$ corresponds to forward sliding (yield). Of the two friction terms, τ_c is of greater importance in accounting for the existence of a well-defined yield stress,[12] pertinent to the quasi-plastic materials of interest here. In this work we will find it mathematically expedient to proceed in the approximation $\mu = 0$, so that Eq. (4) reduces to $\tau_* = \tau_P - \tau_c$.

Equation (4) implies the existence of a residual shear stress on the fault at completion of contact.[12] If $\tau_* \leq \tau_c$, no reverse sliding occurs during unloading (low *P*), and the net stress τ_* attained at peak loading persists after contact. If reverse sliding occurs (high *P*), τ_* reduces to τ_c at full unloading. For simplicity, we will assume the former condition, and justify this assumption later (Section VII).

Inclusion of the frictional terms τ_c and μ in Eq. (4) contains provision for fatigue, by attrition of the τ_f term and consequent enhancement of τ with progressive sliding.[37]

(2) Fracture Mechanics

As indicated, the net shear generates stress concentrations at the fault ends in Fig. 8, initiating wing cracks approximately
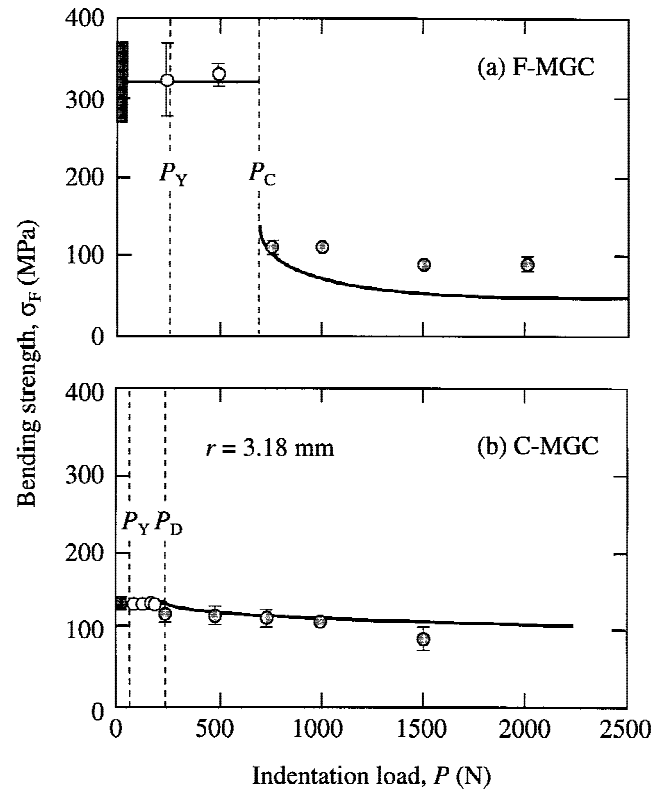

Fig. 6. Strength degradation of Hertzian-indented glass-ceramics as a function of contact load: (a) *F*-MGC, failure from ring cracks; (b) *C*-MGC, failure from shear faults. Indentations with WC sphere, *r* = 3.18 mm. Four-point bend-strength specimens, 3 mm × 5 mm × 25 mm with polished surfaces and chamfered and polished edges. Tests in fast loading (<10 ms) in inert environment (silicone oil) to avoid slow crack growth effects. Data points are experimental measurements, error bars indicating standard deviations for three to five specimens: closed symbols represent failures from indentation origins, open symbols from other origins. Shaded box at left axis represents strengths of polished, unindented specimens. Vertical dashed lines indicate threshold loads P_C for cracking, P_Y for yield, and P_D for first degradation. Solid curves are theoretical fits.

parallel to the major compression axis.[13–17,38] Treatments by Horii and Nemat-Nasser[14] and other[16,17] smooth out complications from the kink geometry by replacing the fault with a concentrated line force acting at the edge of the fault, and treating the ensuing wing crack as a reinitiation problem. Horii and Nemat-Nasser[14] introduce an "effective crack length" correction term to allow for the nonzero fault size. Another approach considers the shear fault and extensile crack as part of
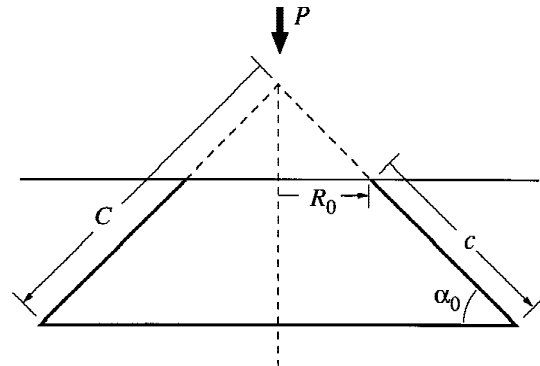

Fig. 7. Model for ring crack formed at contact load *P*. The system is treated as a penny crack of virtual radius $C = c + R_0/\cos \alpha_0$.
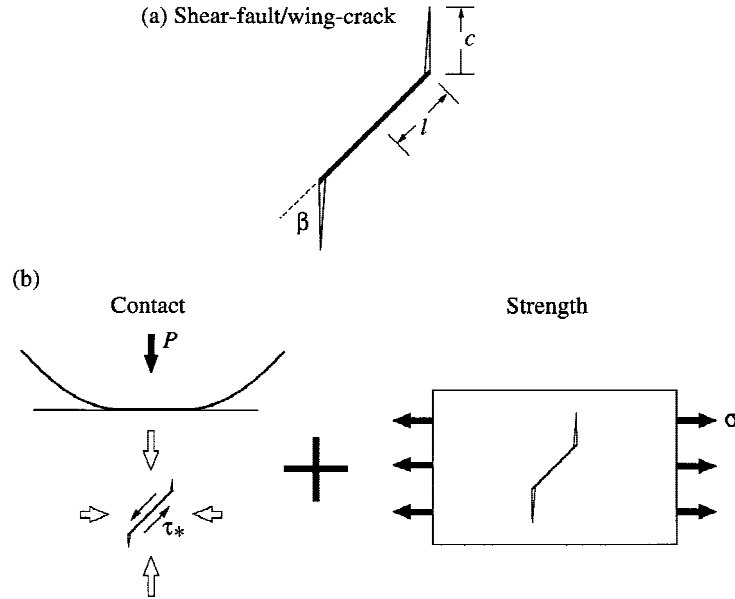
Fig. 8. Model for extension of wing crack from shear fault. (a) Coordinate system. Composite crack is treated as pennylike with virtual radius $C = c + \gamma l$ ($\gamma = 0.27$), c annular wing crack radius and l fault radius. (b) Two-step indentation–strength sequence: compression field at contact load P forms fault with residual shear stress τ_*; subsequent application of tensile stress σ takes crack to failure.

an integral penny-crack system, with superposable stress-intensity factors from each component of resolved stress acting on the fault and crack segments.[38,39] We adopt a hybrid approach here, in an effort to provide a simple solution without compromising essential features of the strength response.

Accordingly, we consider the composite shear-fault/wing-crack system in Fig. 8 as a planar penny crack with center loading from the residual stresses on the shear fault, of effective radius

$$C = c + \gamma l \qquad (5)$$

where c is the annular wing crack width and l the shear fault radius, and γ is a dimensionless geometry coefficient. In the manner of Horii and Nemat-Nasser,[14] γl may be viewed as a correction term to allow for the contribution of the fault surface to the effective length of the composite crack—those authors determine $\gamma = 0.27$. As we shall show, this term usefully allows us to express the conditions for crack initiation and propagation in a unified formulation. The net shear stress τ_* over the fault area gives rise to an opening center force Q on the unloaded crack,[12]

$$Q = \lambda l^2 \tau_* \qquad (6)$$

with λ a dimensionless coefficient. Again, Eq. (6) holds only if $\tau_* \le \tau_c$, such that no reverse sliding occurs; if $\tau_* > \tau_c$, so that reverse sliding does occur, Q reduces to $Q_0 = \lambda l^2 \tau_c$.[12] We will confirm later that the latter state is not attained in the case studies considered here (Section V).

The persistence of the force Q imposes a residual mode I stress-intensity factor on the crack in Fig. 8, somewhat akin to the intrinsic "microstructural driving force" envisaged by Cook et al.[40] The residual K-field may be written in the same equilibrium form as Eq. (2):

$$K_F = \chi Q / C^{3/2} = T_0 \qquad (7)$$

(3) Strength

Now suppose that the residual fault/crack system is subjected to an applied tensile stress σ, Fig. 8. The net stress-intensity factor on the composite crack is made up of mode I contributions K_F from the residual force Q (Eq. (7)) and K_A from the applied tension σ:

$$K = K_F + K_A = \chi Q / C^{3/2} + \Psi \sigma C^{1/2} = T_0 \qquad (8)$$

at equilibrium, with T_0 the toughness of the material through which the wing crack propagates (e.g., grain boundary in polycrystal, matrix phase in ceramic with platelet inclusions). Substituting Eq. (6) and defining the dimensionless quantities

$$\mathscr{C} = C/l \qquad (9a)$$

$$\mathscr{S} = \psi \sigma l^{1/2} / T_0 \qquad (9b)$$

$$\mathscr{T}_* = \chi \lambda \tau_* l^{1/2} / T_0 \qquad (9c)$$

Equation (8) transposes to a normalized expression for $\mathscr{S}(\mathscr{C}, \mathscr{T}_*)$:

$$\mathscr{S} = (1/\mathscr{C}^{1/2})(1 - \mathscr{T}_*/\mathscr{C}^{3/2}) \qquad (10)$$

Plots of $\mathscr{S}(\mathscr{C})$ for specified values of $\mathscr{T}_*$ are shown in Fig. 9. These functions have maxima at

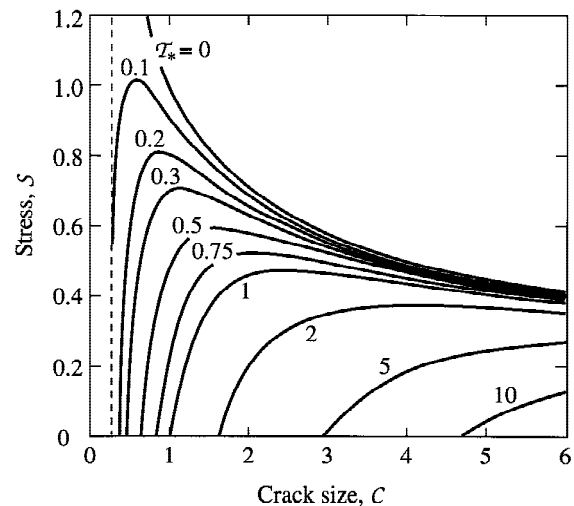**Fig. 9.** Normalized plot of applied tensile stress $\mathscr{S}$ as function of crack length $\mathscr{C}$ for extension of wing crack, at specified residual shear stresses $\mathscr{T}_*$. Vertical dashed line at $\mathscr{C} = \gamma = 0.27$ denotes virtual edge of shear fault from which wing cracks extend. In range $\mathscr{T}_* > 0.035$ cracks extend stably to maximum in curve prior to failure.

$$\mathscr{C}_M = (4\mathcal{T}_*)^{2/3} \qquad (11a)$$

$$\mathscr{S}_M = 3/[4(4\mathcal{T}_*)^{1/3}] \qquad (11b)$$

Included in Fig. 9 is the vertical dashed line $\mathscr{C} = \gamma = 0.27$ representing $c = 0$ in Eq. (5), i.e., the edge of the shear fault from which the lengths of the wing cracks are measured. Note, however, that $\mathscr{C}_M$ and $\mathscr{S}_M$ in Eq. (11) are independent of γ.

The curves in Fig. 9 show how the strength responses vary with the level of residual shear stress $\mathcal{T}_*$ on the fault. The maximum falls to the right of the dashed line, i.e., $\mathscr{C}_M > 0.27$, corresponding to $\mathcal{T}_* > 0.035$ in Eq. (11a). Within this region the crack grows stably with increasing $\mathscr{S}$ prior to failure, and the normalized strength is given directly by $\mathscr{S}_F = \mathscr{S}_M$ in Eq. (11b). Note two distinct subregions, delineated by the condition $\mathscr{S} = 0$ at $\mathscr{C} = 0.27$, corresponding to $\mathcal{T}_* = 0.14$ in Eq. (10): ''subthreshold activated,'' within $0.035 < \mathcal{T}_* < 0.14$, where a wing crack initiates during tensile loading prior to failure; ''postthreshold activated,'' within $\mathcal{T}_* > 0.14$, where a wing crack initiates during the preceding contact cycle. There is a region beyond the contact yield point at $0 < \mathcal{T}_* < 0.035$ (not represented in Fig. 9) where failure is ''spontaneous'' from the fault edge $\mathscr{C} = \gamma = 0.27$ during stressing, with the strength given by $\mathscr{S}_F = \mathscr{S}(\gamma, \mathcal{T}_*)$ in Eq. (10).

Accordingly, the strength $\sigma_F = \sigma_M$ over the bulk of the τ_* range beyond the contact yield point may be deconvoluted from Eq. (11b) by inserting Eqs. (9b) and (9c) to obtain

$$\sigma_F = (3/4\Psi)(T_0^4/4\chi\lambda l^2\tau_*)^{1/3} \qquad (12)$$

This constitutes our basic strength relation for the data analysis to follow (Section V).

Equation (12) holds above a critical degradation residual stress $\tau_* > \tau_D$, where the wing crack constitutes the dominant flaw in the strength specimen. At $\tau_* < \tau_D$, the strength σ_F is equal to the natural (unindented) strength σ_0, independent of τ_*.

(4) Hertzian Field

Thus far we have considered the mechanics for a composite shear-fault/wing-crack within a volume element in a uniform stress field. This yields the relation in Eq. (12) for strength in terms of the residual shear stress on the fault, $\sigma_F(\tau_*)$. Here we concern ourselves with the strength response in nonuniform Hertzian contact fields. Specifically, we seek a relation for the strength as a function of contact load, $\sigma_F(P)$. As indicated in Fig. 8, failure is expected to occur from a critical fault located beneath the contact along the symmetry axis, with the fault plane oriented close to 45° to this axis, where the shear stresses are greatest; and with the effective wing crack plane closely orthogonal to the tensile stress σ. We assume that the fault–crack system is sufficiently small relative to the scale of the damage zone that the stress gradients over its diameter may be considered negligibly small.

This leaves us to determine a connecting relation $\tau_*(P)$ for a given material system and sphere radius. An analytical expression for this function is not feasible for quasi-plastic solids,

because of the high degree of nonlinearity in the indentation stress–strain responses. Accordingly, we are forced to resort to finite element modeling (FEM) of the contact stress fields to determine this relation. Details of such modeling, using a critical shear stress condition for yield, have been described elsewhere.[26] Computations have been carried out for the specific C-Si$_3$N$_4$[24] and C-MGC materials under consideration here.[25] The FEM procedure begins with a predetermination of input parameters for any given material, by independent measurement and by best-fitting indentation stress–strain curves.[26] The maximum principal shear stress within the contact zone is then evaluated from the algorithm at specified load intervals, giving $\tau_P(P)$. In the spirit of our approximation $\mu = 0$ in Eq. (4), we may then invoke the uniaxial yield stress relation $Y = 2\tau_c$ (Ref. 12) to evaluate $\tau_*(P) = \tau_P(P) - Y/2$.

V. Theoretical Fits to Strength Data

We now apply the above analyses to the strength degradation data for Si$_3$N$_4$ in Fig. 5 and MGC in Fig. 6, for failure from both ring cracks in the F materials and shear-fault/wing-cracks in the C materials. Detailed descriptions of appropriate parameter calibrations of the materials, in conjunction with FEM analyses, are available in separate studies.[24,25] Only a brief description of these calibrations is given here. Results are summarized in Table II.

(1) Fine Microstructures—Failure from Ring Cracks

For predictive evaluation of failure from ring cracks in the F-Si$_3$N$_4$ and F-MGC materials, the following parameters in Eqs. (1) to (3) are predetermined as follows: (i) cone angle α_0 in Eq. (1), from section micrographs (e.g., Figs. 1(a) and 2(a)); (ii) surface ring crack radius R_0 in Eq. (1), from direct measurements of surface traces at critical load P_C (note R_0 does not expand at higher load, even though the contact radius does, and may even engulf the first, inner surface ring cracks and initiate new, outer rings); (iii) toughness T_0 in Eq. (3), from independent Vickers indentation tests; (iv) coefficient χ in Eq. (2), from measurement of virtual cone sizes at different loads, $C(P)$ (together with T_0) (Appendix A); (v) coefficient $\Psi = \Psi(\alpha_0)$ in Eq. (3), from a theoretical evaluation of crack reinitiation within the tensile field at the cone base[19] (Appendix A).

The resulting calculated functions $\sigma_F(P)$ are included as the solid curves for F-Si$_3$N$_4$ and F-MGC in Figs. 5(a) and 6(a). The horizontal lines at $P < P_C$ in those figures correspond to the mean natural (unindented) strengths σ_0 for each material (Table II). The curves at $P > P_C$ correspond to the cone crack predictions from Eqs. (1) to (3). The predicted curves account for the extent of the strength loss at $P = P_C$, and provide lower bounds for the subsequent degradation at higher loads.

(2) Coarse Microstructures—Failure from Shear Faults

The microscopic shear-fault/wing-cracks in the C-Si$_3$N$_4$ and C-MGC materials are less accessible to direct measurement. Accordingly, calibration of Eq. (12) for strength evaluation in

Table II. Material Variables for Ceramics Used in This Study

Material	F-Si$_3$N$_4$	C-Si$_3$N$_4$	F-MGC	C-MGC
Natural strength, σ_0 (MPa)	885	792	304	126
Toughness, T_0 (MPa·m$^{1/2}$)	3.9		0.9	
Young's modulus, E (GPa)	335	315	69	49
Poisson's ratio, ν	0.27	0.29	0.25	0.25
Yield stress, $Y = 2\tau_c$ (GPa)		7.3		0.9
Strain-hardening coeff, α		0.5		0.2
Ring crack radius, R_0 (μm)	310 ($r = 2.38$ mm)		360 ($r = 3.18$ mm)	
Ring crack angle, α_0 (deg)	19.0		18.5	
Critical ring crack load, P_C (N)	2100		700	
Critical yield load, P_Y (N)		1300		75
Degradation load, P_D (N)		2600		240
Cone crack coeff, Ψ	0.71		0.79	
Cone crack coeff, χ	15.4×10^{-3}		16.0×10^{-3}	

the coarse structures is conducted in a more empirical manner, using FEM to determine the dependence $\tau_*(P)$[26] and thus to generate the full strength degradation function $\sigma_F(P)$.

To determine $\tau_*(P)$, we use an elastic–plastic constitutive uniaxial stress–strain relation, in accordance with a critical shear stress condition for yield, in the FEM algorithm (Appendix B), with the following input parameters (Table II): (i) elastic parameters, Young's modulus E and Poisson's ratio ν, from sonic measurements; (ii) yield stress Y, from measurements of $P_Y = \pi a^2 p_Y = 1.1\pi a^2 Y$ in Figs. 5(b) and 6(b);[41] (iii) linear strain-hardening coefficient α, which quantifies the degree of quasi-plasticity, by best-fitting indentation stress–strain curves[26] (Appendix B).

Functions $\tau_P(P)$ obtained in this way for C-Si$_3$N$_4$[31] and C-MGC[25] are plotted in Fig. 10. The horizontal dashed lines at $\tau_P = \tau_c = Y/2$ represent the onset of yield, corresponding to $\tau_* = 0$. The vertical dashed lines represent the loads $P = P_D$ (Figs. 5(b) and 6(b)), from which we may directly evaluate the residual shear stresses $\tau_* = \tau_D$ at which degradation first occurs (Table II). The function $\tau_P(P)$ is bounded by curves for hypothetical extremes: fully elastic ($\alpha = 1$), upper dashed curves, calculated from the Hertzian elasticity equations; fully plastic ($\alpha = 0$), given by the horizontal dashed line through $\tau_P = \tau_c$. Note that the functions $\tau_*(P) = \tau_P(P) - \tau_c$ that derive from the plots in Fig. 10 satisfy the condition $\tau_* < \tau_c$ for zero reverse sliding assumed in Section IV.

An empirical fit to the FEM-generated functions (Appendix B) yields the approximate result

$$\tau_*/\tau_c = \alpha[P/P_Y)^{1/3} - 1] \qquad (P > P_Y) \qquad (13)$$

Inserting the natural strength $\sigma_F = \sigma_0$ at $\tau_* = \tau_D$ into Eq. (12) yields

$$\sigma_F/\sigma_0 = (\tau_D/\tau_*)^{1/3} \qquad (14)$$

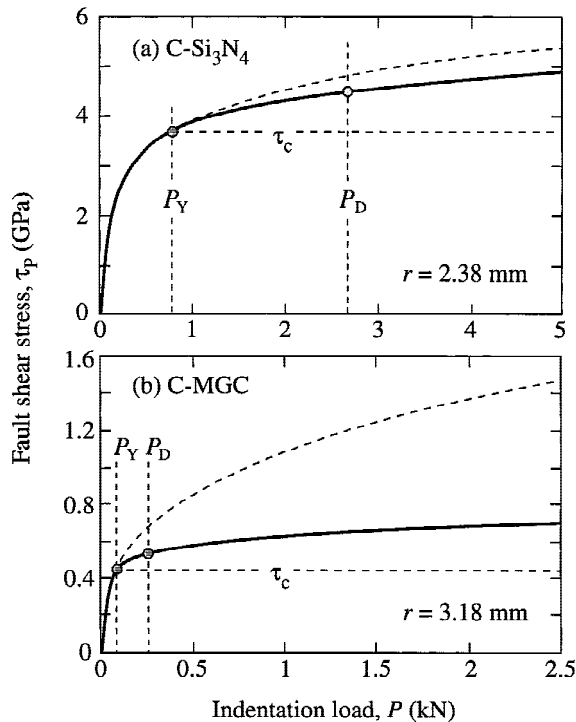Identifying $\tau_* = \tau_D$ with $P = P_D$ in Eq. (13), and combining

Fig. 10. FEM-generated maximum shear stress τ_P on faults within Hertzian contact zone as function of contact load P for coarse microstructures, for WC sphere radius specified: (a) C-Si$_3$N$_4$ and (b) C-MGC. Critical loads for onset of yield, $P = P_Y$, and degradation, $P = P_D$, indicated.

with Eq. (14), we obtain an explicit expression for the strength degradation:

$$\sigma_F = \sigma_0[(P_D^{1/3} - P_Y^{1/3})/(P^{1/3} - P_Y^{1/3})]^{1/3} \qquad (P > P_D) \quad (15)$$

The resultant strength–load functions $\sigma_F(P)$ for C-Si$_3$N$_4$ and C-MGC, using the measured values of P_Y and P_D, are included as the solid curves in Figs. 5(b) and 6(b). Again, the horizontal lines at $P < P_D$ correspond to the mean natural strengths σ_0 for each material (Table II). The fits account for the continuous, ultraslow strength falloff.

VI. Microcrack Coalescence

So far we have assumed that failure occurs from a single microcrack. What happens when the fault density N becomes sufficiently large that coalescence with neighboring cracks occurs before a potentially critical wing crack attains instability during the strength test? The prospect of coalescence increases as the characteristic separation $d \approx 1/2N^{1/3}$ reduces toward the crack diameter C (Fig. 11), with attendant catastrophic falloff in strength. Such a catastrophic falloff is not in evidence in Figs. 5 and 6, but has been observed in repeat contact experiments.[9,25]

For any given residual shear stress τ_* (or contact load P), the condition for coalescence is that a stably extending crack should intersect its neighbor before satisfying the instability condition. Ignoring crack–crack interactions in the stress-intensity factors, this condition is simply $\mathscr{D} \leq \mathscr{C}_M$, where $\mathscr{D} = d/l$ (cf. Eq. (9a)). With Eq. (11), this condition corresponds to $\mathscr{D} \leq (4\mathscr{T}_*)^{2/3}$. The strength within this coalescence region is then given by inserting $\mathscr{C} = \mathscr{D}$, $\mathscr{S} = \mathscr{S}_F$ into Eq. (10):

$$\mathscr{S}_F = (1/\mathscr{D}^{1/2})(1 - \mathscr{T}_*/\mathscr{D}^{3/2}) \qquad (\mathscr{T}_* > \mathscr{D}^{3/2}/4) \qquad (16)$$

predicting a linear falloff with respect to $\mathscr{T}_*$ in $\mathscr{S}_F(\mathscr{T}_*)$. To highlight this falloff, we plot $\mathscr{S}_F(\mathscr{T}_*)$ in Fig. 11 in logarithmic coordinates, for three selected values of $\mathscr{D}$.

In principle, the falloff in Fig. 11 continues to the $\mathscr{T}_*$ axis, to zero strength. In reality such degradation is usually limited, because the microcracks usually only propagate to the boundary of the damage zone (or perhaps a little beyond, in extreme cases), producing strength levels more like those from fully developed radial cracks.[9,25] Nevertheless, such falloff spells the beginning of the end for the useful lifetime of these materials, if not from strength degradation then by excessive material removal.

VII. Discussion

In this paper we have developed models for strength degradation in Hertzian contacts: from ring cracks in fine (F), homogeneous structures (brittle response); and from microdamage cracks in coarse (C) heterogeneous structures (quasi-plastic response). In both cases we have represented the cracks as ''virtual'' pennies, to simplify and accommodate geometrical complexities. Theoretical fracture mechanics then yields appropriate strength–load functions $\sigma_F(P)$ in the degradation region, and identifies controlling material variables. Silicon nitride (Si$_3$N$_4$) and micaceous glass-ceramic (MGC) microstructures (Table I) afford illustrative case studies for data analysis (Table II).

Essential features of the models for the F and C structure types are as follows:

(i) F structures. Failure occurs from truncated cone cracks. The fracture mechanics relations Eqs. (1) to (3) make due allowance for the truncation (Fig. 7), specifically for the location of the virtual tip above the indented surface, with consequent improvement in data fitting relative to earlier models.[19] These equations account for the abrupt falloff in strength at the critical contact load P_C, and slow falloff thereafter at $P > P_C$ (Figs. 5(a) and 6(a)). From direct measurements of P_C, surface ring crack radius R_0, and crack angle α_0, all of the
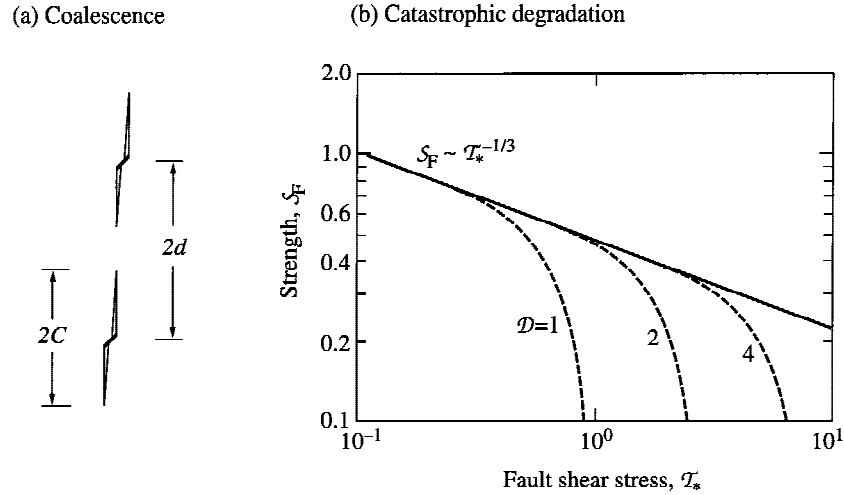
Fig. 11. Coalescence of wing cracks: (a) coordinate system; (b) plot of normalized strength $\mathscr{S}_F$ as function of residual shear stress $\mathscr{T}_*$ for wing crack extension (solid curve), showing coalescence-associated falloff for specified values of microcrack separation D.

geometrical coefficients in Eqs. (1) to (3) can be experimentally predetermined, conferring the model with a certain predictive capability. The fact that the data points at higher loads in Figs. 5(a) and (especially) 6(a) lie above the predicted curves at $P > P_C$ may be attributable to engulfment of the surface ring cracks by the ever-expanding contact circle, leading to arrest of the inner ring cracks and the initiation of multiple cones.[24]

(ii) C structures. Failure occurs from individual shear-fault/wing-cracks within the damage zone population (Fig. 8). The model accounts for the relatively continuous falloff in strength at P_D, and even slower falloff (relative to F structures) at $P > P_D$ (Figs. 5(b) and 6(b)). At the same time, the model allows for catastrophic loss from crack coalescence at extreme loads (or, potentially, numbers of cycles). Interesting inclusions in the formation are the residual fault driving force Q (Eqs. (7) and (8)) and the fault-length contribution γl to the net size of the virtual crack C in Eq. (5). The point force Q provides a stabilizing influence on the crack growth prior to failure, with progressively enhanced extension ($\mathscr{C}_M$) and diminished strength ($\mathscr{S}_M$) at increasing residual stress ($\mathscr{T}_*$). This kind of stabilization is common in indentation problems.[42,43] However, while γ modifies the actual crack length, it does not feature in Eq. (12), so the strength is insensitive to the value of this parameter. Parametric calibration of Eq. (15) involves measurement of the load P_Y at first yield, and of the load P_D at first strength degradation below σ_0. Because of the empirical nature of this latter adjustment, Eq. (15) is not amenable to *a priori* predictions of $\sigma_F(P)$.

A key element of the study is the role of microstructure in determining the fundamental mechanism of the strength degradation, by controlling the degree of quasi-plasticity. In the materials chosen for examination here[24,25] the brittle–plastic transition is effected primarily by grain coarsening and elongation, with intrinsic provision for shear-activated faulting at weak internal interfaces.[8] The single material parameter that most compellingly quantifies this transition is the strain-hardening coefficient α (a measure of the density of active faults within the contact compression–shear zone[12]) in the constitutive stress–strain relation used in the FEM computations (Appendix B). The effect of reducing this parameter between the bounds $\alpha = 1$ (full elasticity) and $\alpha = 0$ (full plasticity) is to depress the $\tau_*(P)$ curve (Fig. B2, Appendix B), rendering the ceramic structure less susceptible to abrupt strength losses as ring cracking is suppressed in favor of quasi-plastic deformation. For the C materials, inserting $\tau_* = \tau_D$ at $P = P_D$ into Eq. (13) yields $P_D/P_Y = [(\tau_D/\alpha\tau_c) + 1]^3$, so that reducing α increases P_D (recall τ_D is constant at fixed σ_0 in Eq. (14)), shifting $\sigma_F(P)$ to higher loads in Eq. (15) and diminishing the degradation further.

The fault–crack model for C structures provides approximate bounding solutions for crack initiation and coalescence during the initial contact cycle, as starting conditions for the strength test. The critical condition $\tau_* = \tau_i$ for contact-induced wing crack initiation is $K_F = T_0$ at $c = 0$ in Eqs. (5) to (7), yielding

$$\tau_i = (\gamma^{3/2}/\chi\lambda)T_0/l^{1/2} \qquad (17)$$

i.e., a Hall–Petch relation in fault size.[38] Note that incorporation of the fault "correction" term γ is paramount here—to ignore the fault is to imply spontaneous initiation (i.e., $\gamma = 0$, $\tau_i = 0$). The size C_0 of the resulting wing cracks beyond the initiation stress level is obtained from Eqs. (6) and (7):

$$C_0 = (\chi\lambda l^2 \tau_*/T_0)^{2/3} \qquad (\tau_* > \tau_i) \qquad (18)$$

corresponding to the appropriate intercept along the $\mathscr{C}$ axis in Fig. 9. The critical condition $\tau_* = \tau_D$ for contact-induced coalescence ("disintegration") at high fault densities (Fig. 10) is given by equating $C_0 = d$ in Eq. (18), giving

$$\tau_D = T_0 d^{3/2}/\chi\lambda l^2 \qquad (19)$$

indicating upper practical limits to the concentration of shear faults ($N \approx 1/8d^3$) and grain size (l) in heterogeneous microstructures.

In this paper we have presented data using a single sphere radius r for each material. How do the strength characteristics in Figs. 5 and 6 depend on variations in r? Indentation damage modes are renowned for their strong size effects.[34] Generally, as the indenter radius is reduced, fracture is progressively suppressed relative to plasticity, enhancing any brittle–plastic transition.[44–46] With the ring crack mode, the main effect is felt in the critical load where the strength undergoes its abrupt decline, generally with a sphere size dependence somewhere between $P_C \propto r$ and $P_C \propto r^2$.[32,33,47] A secondary effect is felt in the ensuing degradation at $P > P_C$, via some scaling of r with the surface ring crack radius R_0 in Eq. (1). With the quasi-plasticity mode, the yield response in monolithic materials usually satisfies the requirements of geometrical similarity, expressible as $P_Y \propto r^2$, $P_D \propto r^2$,[41] with the associated shear stresses τ_c and τ_D invariant. A more complete analysis of sphere-size effects in the analysis of strength degradation of Si_3N_4 will be given elsewhere.[24]

Some limitations in our model for quasi-plastic ceramics are acknowledged. In the fracture mechanics analysis we have assumed an annular pennylike geometry for the wing crack, with $c^{-3/2}$ falloff in K_F in Eq. (7); others have assumed a line-crack geometry with extension confined to the top and bottom ends of the fault,[13–17] and with $c^{-1/2}$ falloff. The latter dependence would result in a faster strength falloff in $\sigma_F(P)$. Actual behav-

ior probably lies somewhere between these two bounds. We have assumed that the fault undergoes no reverse sliding during contact ($\tau_* < \tau_c$), so that the net shear stress τ_* on the shear fault at maximum load persists on unloading. If reverse sliding were to occur ($\tau_* > \tau_c$), then τ_* would relax back to τ_c at full unload.[12] And since τ_c is independent of P, the strength degradation would saturate. However, the condition $\tau_* > \tau_c$ is not achieved in either material investigated here (Fig. 10). In dealing with the friction stress τ_f in Eq. (1) we have expediently omitted the μ term. The presence of this term would suppress sliding somewhat during the expanding contact, i.e., lower τ_*, further complicating the $\tau_*(P)$ relations derived from the FEM computations. We have neglected any internal residual mismatch stresses acting on the cracks. Such stresses, which can be substantial in ceramics, would shift the strength curves $\sigma_F(\tau_*)$ up (compression) or down (tension) in Fig. 10. We have taken the toughness of our materials to be single-valued, on the basis that the wing-crack extensions are only on the microscopic scale, whereas in reality heterogeneous ceramics with coarse structures exhibit R-curves. Also, crack–crack interactions in the stress-intensity factor formulation of Section IV have been ignored. Although these interactions are generally not substantial until the crack separations are very small,[48] they could be significant in the coalescence condition in Section VI. Finally, in determining the empirical relation Eq. (13) we have ignored deformation of the spherical indenter, which occurs in tests on harder ceramics like Si_3N_4.[24,26] All these limitations, taken together with the empirical nature of our calibrations for the C materials in Section V, especially in relation to the function $\tau_*(P)$, lend the model a somewhat phenomenological flavor. In this context, absolute values for some of the calibrated parameters should not be taken too literally. At the same time, the theoretical strength degradation function in Eq. (15) is not highly sensitive to P, and accounts for all the broader data trends.

With this last qualification, the model is well placed for extension to contact fatigue.[37] This is accommodated by attrition of τ_f in Eq. (1), specifically the friction parameters τ_c and/or μ, leading to a progressive increase in τ_*.[12] An optimum condition for attrition would appear to be reverse sliding at the faults during unloading,[37] i.e., $\tau_* > \tau_c$. In the present experiments the progressive yield within the quasi-plastic damage zone limits the build up of τ_* to levels well below τ_c (Fig. 10). Yet accelerated strength loss in repeat loading apparently does occur in heterogeneous ceramics over the load range represented here.[25,37] This raises the issue of stochastics: real ceramics are inevitably characterized by a distribution in fault-sizes, so the yield condition is subject to a statistical element.[6] It needs only one particularly large fault to activate below the nominal yield stress in order for degradation to occur. The issue of fatigue in these quasi-plastic materials will be pursued elsewhere.

APPENDIX A

Evaluation of Cone Crack Parameter Ψ

Evaluations of the two geometrical coefficients in the ring-crack formulation listed for the F materials in Table II, χ in Eq. (2) and Ψ in Eq. (3), are made using data from separate studies.

Figure A1 plots C vs $P^{2/3}$ from measured values of $c(P)$ in conjunction with Eq. (1), for F-Si_3N_4[24] and F-MGC.[25] Asymptotic data fits yield the values of $\chi = T_0C^{3/2}/P$ (Eq. (2)) listed in Table II.

Figure A2 is a plot of Ψ as a function of cone angle α_0, which depends on Poisson's ratio.[49,50] The function $\Psi(\alpha_0)$ is determined from an analogous function $\Omega(\alpha_0)$, with $\Psi = (\Omega\pi)^{1/2}$, generated from a detailed fracture mechanics analysis of crack initiation at the cone base in an applied tensile field (tensile axis normal to cone axis).[19] The values of Ψ are then determined at the measured crack angles α_0 in Table II.
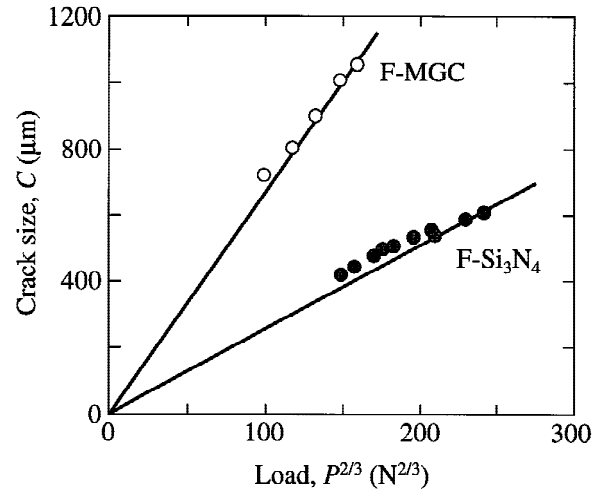

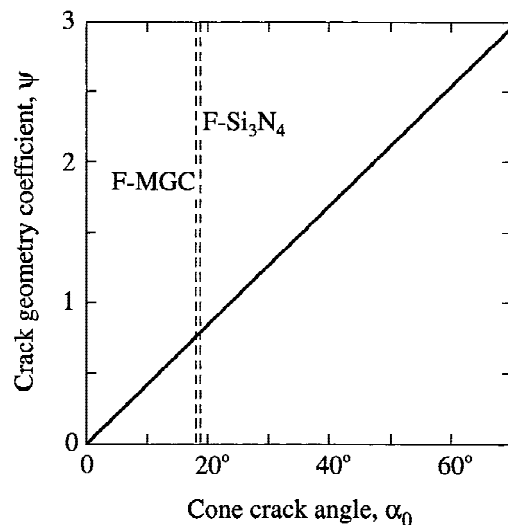**Fig. A1.** Plots of C vs $P^{2/3}$ for F-Si_3N_4 (data from Ref. 24) and F-MGC (data from Ref. 25.)

Fig. A2. Crack geometry coefficient Ψ as a function of cone angle α_0 (generated from Ref. 19). Angles for F-Si_3N_4 and F-MGC indicated.

APPENDIX B

FEM Evaluation of Elastic–Plastic Contact Field

The starting points for finite element modeling (FEM) evaluations of the function $\tau_*(P)$ in Section V (2) are indentation stress–strain curves, which plot mean contact pressure p_0 (indentation stress) against a/r (indentation strain). Such stress–strain curves for C-Si_3N_4[24] and C-MGC[25] are shown in Fig. B1. Note that the curve for C-MGC is considerably lower and flatter than that for C-Si_3N_4, indicating a much softer material.

Models of frictional sliding at shear faults in applied uniform compression fields σ_A predict a linear strain-hardening relation between uniaxial stress σ_A and strain ε_A[12,26]

$$\sigma_A = Y + \alpha(\varepsilon_A E - Y) \qquad (\sigma_A > Y) \qquad \text{(B-1)}$$

with E Young's modulus and Y yield stress, in accordance with a critical shear stress criterion for slip. Equation (B-1) is used as a constitutive relation for the FEM analysis. The FEM algorithm assumes a frictionless contact between WC sphere and specimen surface, and contains provision for deformation of
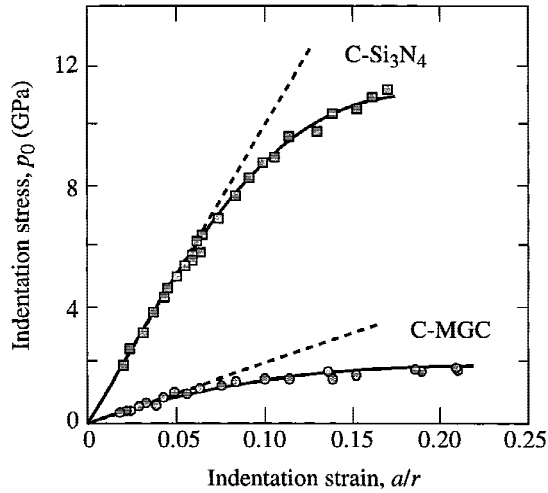
Fig. B1. Indentation stress–strain curves for F-Si$_3$N$_4$ (data from Ref. 24) and F-MGC (data from Ref. 25). Solid curves are FEM fits. Dashed lines are bounds from Hertzian elasticity solutions.
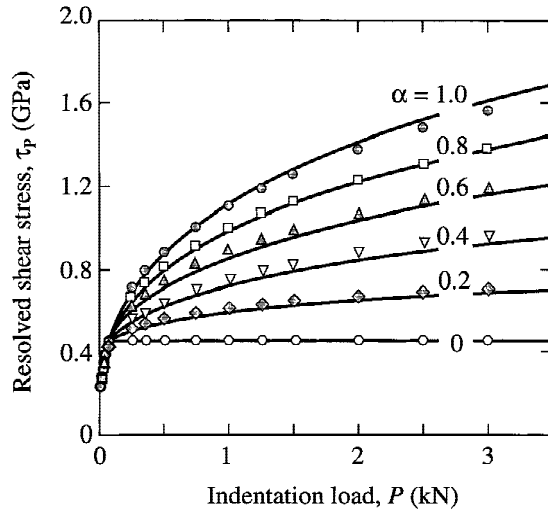

Fig. B2. Plots of function $\tau_P(P)$ for C-MGC at $r = 3.18$ mm. Data points generated from FEM algorithm, for selected hypothetical values of strain-hardening coefficient α. Solid curves are corresponding functions from empirical relation Eq. (B-2).

the sphere (essential with harder materials like Si$_3$N$_4$).[26] Input elasticity parameters are E and ν, plasticity parameters Y and α. Here, all parameters are obtained by independent means, except α, which is adjusted to fit the stress–strain curves. Such fits are included as the solid curves in Fig. B1.

 With these parameter calibrations, the FEM algorithm enables evaluation of the maximum shear stress τ_P along the symmetry axis, at depth $\approx 0.5a$ (a contact radius). Resulting values of τ_P at increments of load P for the C-MGC materials, but for a series of hypothetical α values, are plotted as data points in Fig. B2. Above $P = P_Y$ these data appear to scale with α, with lower bound at $\tau_P = \tau_c$ = constant and upper bound at $\tau_P = \tau_c(P/P_Y)^{1/3}$ (Hertzian elasticity solution).[51] Accordingly, writing $\tau_* = \tau_P - \tau_c$, we fit an empirical function

$$\tau_*/\tau_c = \alpha[(P/P_Y)^{1/3} - 1] \tag{B-2}$$

to the intervening data in Fig. B2.

 A similar analysis for the harder C-Si$_3$N$_4$ material reveals analogous trends, but is complicated by effects from deformation of the WC sphere at the higher α values. Then Eq. (B-2)

overestimates τ_*/τ_c, so the strength degradation relation in Eq. (15) is conservative.

 The resulting $\tau_*(P)$ functions for C-Si$_3$N$_4$ and C-MGC using actual calibrated values of α from Table II are plotted as the solid curves in Fig. 10.

References

[1]J. W. Lucek, ''Rolling Wear of Silicon Nitride Bearing Materials''; ASME Paper No. 90-GT-165 in *Gas Turbine and Aeroengine Congress and Exposition*. Brussels, Belgium, 1990.

[2]R. N. Katz and J. G. Hannoosh, ''Ceramics for High Performance Rolling Element Bearings: A Review and Assessment,'' *Int. J. High Technol. Ceram.*, **1**, 69–79 (1985).

[3]D. W. Richerson, *Modern Ceramic Engineering*. Marcel Dekker, New York, 1992.

[4]I. M. Peterson, A. Pajares, B. R. Lawn, V. P. Thompson, and E. D. Rekow, ''Mechanical Characterization of Dental Ceramics: A Study Using Hertzian Contacts,'' *J. Dent. Res.*, **77** [4] 589–602 (1998).

[5]F. Guiberteau, N. P. Padture, H. Cai, and B. R. Lawn, ''Indentation Fatigue: A Simple Cyclic Hertzian Test for Measuring Damage Accumulation in Polycrystalline Ceramics,'' *Philos. Mag. A*, **68** [5] 1003–16 (1993).

[6]F. Guiberteau, N. P. Padture, and B. R. Lawn, ''Effect of Grain Size on Hertzian Contact in Alumina,'' *J. Am. Ceram. Soc.*, **77** [7] 1825–31 (1994).

[7]H. Cai, M. A. Stevens Kalceff, and B. R. Lawn, ''Deformation and Fracture of Mica-Containing Glass-Ceramics in Hertzian Contacts,'' *J. Mater. Res.*, **9** [3] 762–70 (1994).

[8]B. R. Lawn, N. P. Padture, H. Cai, and F. Guiberteau, ''Making Ceramics 'Ductile','' *Science*, **263**, 1114–16 (1994).

[9]N. P. Padture and B. R. Lawn, ''Contact Fatigue of a Silicon Carbide with a Heterogeneous Grain Structure,'' *J. Am. Ceram. Soc.*, **78** [6] 1431–38 (1995).

[10]H. H. K. Xu, L. Wei, N. P. Padture, B. R. Lawn, and R. L. Yeckley, ''Effect of Microstructural Coarsening on Hertzian Contact Damage in Silicon Nitride,'' *J. Mater. Sci.*, **30**, 869–78 (1995).

[11]N. P. Padture and B. R. Lawn, ''Toughness Properties of a Silicon Carbide with an *In-Situ*-Induced Heterogeneous Grain Structure,'' *J. Am. Ceram. Soc.*, **77** [10] 2518–22 (1994).

[12]B. R. Lawn and D. B. Marshall, ''Nonlinear Stress–Strain Curves for Solids Containing Closed Cracks with Friction,'' *J. Mech. Phys. Solids*, **46** [1] 85–113 (1998).

[13]H. Horii and S. Nemat-Nasser, ''Compression-Induced Microcrack Growth in Brittle Solids: Axial Splitting and Shear Failure,'' *J. Geophys. Res.*, **90** [B4] 3105–25 (1985).

[14]H. Horii and S. Nemat-Nasser, ''Brittle Failure in Compression: Splitting, Faulting and Brittle–Ductile Transition,'' *Philos. Trans. R. Soc. London*, **319** [1549] 337–74 (1986).

[15]M. F. Ashby and S. D. Hallam, ''The Failure of Brittle Solids Containing Small Cracks Under Compressive Stress States,'' *Acta Metall. Mater.*, **34** [3] 497–510 (1986).

[16]J. M. Kemeny and N. G. W. Cook, ''Micromechanics of Deformation in Rock''; pp. 287–311 in *Toughening Mechanisms in Quasi-Brittle Materials*. Edited by S. P. Shah. Kluwer Academic Publishers, Dordrecht, Netherlands, 1991.

[17]A. V. Dyskin, R. J. Jewell, H. Joer, E. Sahouryeh, and K. B. Ustinov, ''Experiments on 3-D Crack Growth in Uniaxial Compression,'' *Int. J. Fract.*, **65** [4] R77–83 (1994).

[18]N. P. Padture, C. J. Evans, H. H. K. Xu, and B. R. Lawn, ''Enhanced Machinability of Silicon Carbide via Microstructural Design,'' *J. Am. Ceram. Soc.*, **78** [1] 215–17 (1995).

[19]B. R. Lawn, S. M. Wiederhorn, and H. Johnson, ''Strength Degradation of Brittle Surfaces: Blunt Indenters,'' *J. Am. Ceram. Soc.*, **58** [9–10] 428–32 (1975).

[20]B. R. Lawn, E. R. Fuller, and S. M. Wiederhorn, ''Strength Degradation of Brittle Surfaces: Sharp Indenters,'' *J. Am. Ceram. Soc.*, **59** [5–6] 193–97 (1976).

[21]S. M. Wiederhorn and B. R. Lawn, ''Strength Degradation of Glass Resulting from Impact with Spheres,'' *J. Am. Ceram. Soc.*, **60** [9–10] 451–58 (1977).

[22]B. R. Lawn and D. B. Marshall, ''Indentation Fracture and Strength Degradation in Ceramics''; pp. 205–29 in *Fracture Mechanics of Ceramics*, Vol. 3. Edited by R. C. Bradt, D. P. H. Hasselman, and F. F. Lange. Plenum, New York, 1978.

[23]B. R. Lawn, S. M. Wiederhorn, and D. E. Roberts, ''Effect of Sliding Friction Forces on the Strength of Brittle Materials,'' *J. Mater. Sci.*, **9**, 2561–69 (1984).

[24]S. K. Lee, S. Wuttiphan, and B. R. Lawn, ''Role of Microstructure in Hertzian Contact Damage in Silicon Nitride: I. Mechanical Characterization,'' *J. Am. Ceram. Soc.*, **80** [9] 2367–81 (1997).

[25]I. M. Peterson, S. Wuttiphan, A. Pajares, and B. R. Lawn, ''Effect of Microstructure on Contact Damage and Strength Degradation in Micaceous Glass-Ceramics,'' *J. Dent. Mater.*, in press.

[26]A. C. Fischer-Cripps and B. R. Lawn, ''Stress Analysis of Contact Deformation in Quasi-Plastic Ceramics,'' *J. Am. Ceram. Soc.*, **79** [10] 2609–18 (1996).

[27]C. K. Chyung, G. H. Beall, and D. G. Grossman, ''Microstructures and Mechanical Properties of Mica Glass-Ceramics''; pp. 1167–94 in *Electron Microscopy and Structure of Materials*. Edited by G. Thomas, R. M. Fulrath, and R. M. Fisher. University of California Press, Berkeley, CA, 1972.

[28]K. Chung, ''Fracture Energy and Thermal Shock Resistance of Mica Glass-Ceramics''; pp. 495–508 in *Fracture Mechanics of Ceramics*, Vol. 2. Edited by R. C. Bradt, D. P. H. Hasselman, and F. F. Lange. Plenum Press, New York, 1974.

[29]D. G. Grossman, ''Structure and Physical Properties of Dicor/MGC Glass-Ceramic''; pp. 103–15 in *Proceedings of the International Symposium on Computer Restorations*. Edited by W. H. Mörmann. Quintessence Publishing Co., Chicago, IL, 1991.

[30]A. C. Fischer-Cripps and B. R. Lawn, ''Indentation Stress–Strain Curves for ''Quasi-Ductile'' Ceramics,'' *Acta Metall.*, **44** [2] 519–27 (1996).

[31]S. K. Lee and B. R. Lawn, ''Role of Microstructure in Hertzian Contact Damage in Silicon Nitride: II. Strength Degradation,'' *J. Am. Ceram. Soc.*, **81** [4] 997–1003 (1998).

[32]F. C. Frank and B. R. Lawn, ''On the Theory of Hertzian Fracture,'' *Proc. R. Soc. London*, **A299** [1458] 291–306 (1967).

[33]B. R. Lawn and T. R. Wilshaw, ''Indentation Fracture: Principles and Applications,'' *J. Mater. Sci.*, **10** [6] 1049–81 (1975).

[34]B. R. Lawn, *Fracture of Brittle Solids*. Cambridge University Press, Cambridge, U.K., 1993.

[35]F. C. Roesler, ''Brittle Fractures Near Equilibrium,'' *Proc. Phys. Soc. London*, **B69**, 981 (1956).

[36]J. C. Jaeger and N. G. W. Cook, *Fundamentals of Rock Mechanics*. Chapman and Hall, London, U.K., 1971.

[37]N. P. Padture and B. R. Lawn, ''Fatigue in Ceramics with Interconnecting Weak Interfaces: A Study Using Cyclic Hertzian Contacts,'' *Acta Metall.*, **43** [4] 1609–17 (1995).

[38]B. R. Lawn, N. P. Padture, F. Guiberteau, and H. Cai, ''A Model for Microcrack Initiation and Propagation Beneath Hertzian Contacts in Polycrystalline Ceramics,'' *Acta Metall.*, **45** [5] 1683–93 (1994).

[39]S. Lathabai, J. Rödel, B. R. Lawn, and T. P. Dabbs, ''Fracture Mechanics Model for Subthreshold Indentation Flaws: I. Equilibrium Fracture,'' *J. Mater. Sci.*, **26**, 2157–68 (1991).

[40]R. F. Cook, B. R. Lawn, and C. J. Fairbanks, ''Microstructure–Strength Properties in Ceramics: I. Effect of Crack Size on Toughness,'' *J. Am. Ceram. Soc.*, **68** [11] 604–15 (1985).

[41]D. Tabor, *Hardness of Metals*. Clarendon, Oxford, U.K., 1951.

[42]D. B. Marshall and B. R. Lawn, ''Residual Stress Effects in Sharp-Contact Cracking: I. Indentation Fracture Mechanics,'' *J. Mater. Sci.*, **14** [8] 2001–12 (1979).

[43]B. R. Lawn, A. G. Evans, and D. B. Marshall, ''Elastic/Plastic Indentation Damage in Ceramics: The Median/Radial Crack System,'' *J. Am. Ceram. Soc.*, **63** [9–10] 574–81 (1980).

[44]B. R. Lawn and D. B. Marshall, ''Hardness, Toughness, and Brittleness: An Indentation Analysis,'' *J. Am. Ceram. Soc.*, **62** [7–8] 347–50 (1979).

[45]K. E. Puttick, ''Energy Scaling, Size Effects and Ductile–Brittle Transitions in Fracture,'' *J. Phys. D: Appl. Phys.*, **12**, L19–23 (1979).

[46]K. Puttick, ''The Correlation of Fracture Transitions,'' *J. Phys. D: Appl. Phys.*, **13**, 2249–62 (1980).

[47]F. B. Langitan and B. R. Lawn, ''Hertzian Fracture Experiments on Abraded Glass Surfaces as Definitive Evidence for an Energy Balance Explanation of Auerbach's Law,'' *J. Appl. Phys.*, **40** [10] 4009–17 (1969).

[48]M. Kachanov, ''Effective Elastic Properties of Cracked Solids: Critical Review of Some Basic Concepts,'' *Appl. Mech. Rev.*, **45** [8] 304–35 (1992).

[49]B. R. Lawn, T. R. Wilshaw, and N. E. W. Hartley, ''A Computer Simulation Study of Hertzian Cone Crack Growth,'' *Int. J. Fract.*, **10** [1] 1–16 (1974).

[50]C. Kocer and R. E. Collins, ''The Angle of Hertzian Cone Cracks,'' *J. Am. Ceram. Soc.*, in press.

[51]K. L. Johnson, *Contact Mechanics*. Cambridge University Press, London, U.K., 1985. □